Supplementary information for

Stretchable and Adhesive Bilayers for Electrical Interfacing

*Yuli Song [1 #], Kai Chen [1 #], Shimeng Chen [1 #], Linyuan Zhang [2], Yaqiang Wang [1], Kai Wu [1] *, Canhua Xu [2] *, Bo Li [1] *, Jinyu Zhang [1], Gang Liu [1], Jun Sun [1]*

1 State Key Laboratory for Mechanical Behavior of Materials, Xi'an Jiaotong University, Xi'an, 710049, P.R. China

2 School of Biomedical Engineering, The Fourth Military Medical University, Xi'an, 710032, P. R. China

* Corresponding authors: E-mail: msewukai@xjtu.edu.cn (K. Wu); canhuaxu@fmmu.edu.cn (C. Xu)；libo1137@xjtu.edu.cn (B. Li)

Table of Contents

1. Materials and fabrication

1.1 Materials

Styrene-ethylene-butylene-styrene (SEBS, Tuftec H1221) was purchased from Asahi KASEI. Polydimethylsiloxane (PDMS, Sylgard 184) was purchased from Dow Corning. EGaIn alloy (75.5% Ga, 24.5% In) was purchased from Hunan Zhongcai Shengte New Material Technology Co., Ltd. Polyurethane (PU) and additional cure silicone rubber (Ecoflex 00-30) was purchased from Smooth-on. Anisotropic conductive film (ACF) tape (ECATT 9703) and VHB ™ 4905 tape were purchased from 3M.

1.2 Fabrication of trilayer sheets

The trilayer sheets consist of a nanoscale SEBS elastomer layer, a SEBS-LM composite layer, and a micron-scale SEBS layer. The nanoscale SEBS layer and the SEBS-LM composite layer constitute the conductive and adhesive bilayer interface.

The detailed fabrication process is described as follows. Two groups of specimens were fabricated, respectively, including (i) the same LM particle diameter d but different LM volume fractions ϕ; (ii) the same ϕ but different d.

1.2.1 Fabrication of trilayer sheets with d = 50 μm but different ϕ

First, the SEBS solution (13 wt.% in toluene) was prepared by mixing 15 g SEBS with 100 ml toluene with magnetic stirring at 50°C for 4 hours. The SEBS solution was then mixed with EGaIn LM at ϕ = 10%, 30%, and 50%, respectively, using a planetary centrifugal mixer (TM-310 SIMADA) rotated at 2500 rpm for 5 min, forming a suspension of LM particles dispersed in the SEBS solution. The SEBS-LM suspension was poured into a glass mold (diameter of 200 mm) and covered with a lid. 2 h still-standing at room temperature allows for the settlement of LM particles. Afterwards, the lid was removed and the toluene was evaporated at room temperature for 5 h. Finally, the trilayer

sheet with a thickness of ~ 300 μm was gently removed from the mold.

1.2.2 Fabrication of trilayer sheets with ϕ = 30% but different d.

To fabricate the suspensions of LM particles with d = 25 and 50 μm, the SEBS solutions were mixed with EGaIn using a planetary centrifugal mixer rotated at 2500 rpm for 15 min and 5 min, respectively.

To fabricate the suspensions of LM particles with d = 1.5 μm, EGaIn (7.98 g) and alcohol (10 ml) were first mixed together in a beaker. The mixtures were then sonicated using an ultrasonic cell disruptor (JY92-IIN, Scientz) at 30% sonication amplitude for 5 min. After that, the beaker containing mixtures was placed in a water bath (65 °C) for 3 h to evaporate the alcohol. Then the SEBS solution was added in the beaker and the mixtures were rotated at 2500 rpm for 5 min using a planetary centrifugal mixer.

The suspensions of LM particles with different d in SEBS solutions can be used to fabricate trilayer sheets, following the same procedure described above.

1.3 Fabrication of soft-soft, soft-rigid, and soft-encapsulation connections

1.3.1 Fabrication of soft-soft connection

The bilayer interface soft-soft connection was obtained by face-to-face pressing two bilayer interfaces (30 mm in length and 10 mm in width) without pastes. The overlapping region has a nominal dimension of 10 mm in length and 10 mm in width. The overlapping region was pressed with a 200 g weight for 1 h.

For comparison, two SEBS/SEBS-LM bilayer interfaces were also connected by using some commercial conductive pastes and tapes with the same size of the overlapping region, including ACF tape, Cu tape (3M Scotch 77802), carbon tape (PELCO Image Tabs) and conductive silver paste (SPI 05001-AB).

For comparison, two PDMS-LM sheets were also used to form soft-soft connection by using commercial conductive pastes and tapes (ACF tape, Cu tape, carbon tape, and conductive silver paste). First, the PDMS prepolymer and curing agent were mixed at a weight ratio of 10:1 using a planetary centrifugal mixer for 5 min. The uncured PDMS was then mixed with EGaIn at ϕ = 30%, and rotated at 2500 rpm for 5 min, forming a suspension of LM particles with d = 50 μm dispersed in the PDMS matrix. The PDMS-LM suspension was poured into a glass mold (diameter of 200 mm) and allowed to stand for 12 h at room temperature to settle the LM particles. The mixtures were cured at 80 °C for 2 h. The as-prepared PDMS-LM sheets are insulated electrically and can be subsequently activated by stretching to 80% strain to form conductive pathways.

1.3.2 Fabrication of soft-rigid connection

First, 300 nm-thick Cu film interconnects were deposited on the rigid/flexible modules (polyimide (PI), silicon, and copper wafers) with 30 mm in length and 10 mm in width by magnetron sputtering. A 20 μm-thick SEBS solution was spin-coated on one side of the rigid/flexible modules, and cured at room temperature for 5 h to evaporate toluene. The thin SEBS layer has a length of 10 mm and a width of 10 mm. A bilayer interface was then pressed onto the spin-coated SEBS, forming SEBS-SEBS connection. After that, another two bilayer interfaces were face-to-face pressed onto this bilayer interface. The overlapping region was pressed with a 200 g weight for 1 h. Finally, the soft-rigid connections were fabricated (Fig. S22a).

1.3.3 Fabrication of soft-encapsulation connection

The soft-encapsulation connection was prepared by directly pressing a 300 μm-thick encapsulation layer (SEBS, PDMS, Ecoflex, PU, and VHB tape) on our bilayer interface (~ 300 μm thickness). Both the bilayer interface and the encapsulation layer have dimensions of 50 mm in length and 10 mm in width. The overlapping region has a length of 30 mm and a width of 10 mm. The

overlapping region was pressed with a 200 g weight for 1 h.

To fabricate PDMS sheets, the PDMS prepolymer and curing agent were mixed at a weight ratio of 10:1 using a planetary centrifugal mixer for 5 min. Mixture was cast on a glass sheet and cured at 80 °C for 2h. To fabricate PU sheets, the PU prepolymer and curing agent were mixed at a weight ratio of 1:1 using a planetary centrifugal mixer for 5 min. Mixture was cast on a glass sheet and cured at room temperature for 12h. To fabricate Ecoflex sheets, the Ecoflex prepolymer and curing agent were mixed at a weight ratio of 1:1 using a planetary centrifugal mixer for 5 min. Mixture was cast on a glass sheet and cured at room temperature for 12 h.

1.4 Fabrication of 2-channel bioelectrode

The 2-channel bioelectrodes with a line width of 0.5 mm were prepared by combining the stencil-printing and the proposed method. A pattern mesh frame made from wood is placed on the glass substrate, and the prepared SEBS-LM solution is deposited on the edge of the mesh. A squeegee is used to press the SEBS-LM solution forcedly through the designed mesh. 2 h still-standing at room temperature in a fume hood allows for the settlement of LM particles. After toluene evaporation and SEBS curing, the 2-channel bioelectrodes were transferred to the cured SEBS.

2. Characterizations

2.1 Microstructure characterization

The surface roughness and three-dimensional morphologies were characterized by confocal laser scanning microscopy (CLSM, OLYMPUS LEXT OLS4000). Cross-sectional morphologies of trilayer architectures were observed by a scanning electron microscope (SEM, ZEISS SIGMA 300) equipped with an Oxford energy dispersive X-ray spectroscopy (EDS) system. To characterize the deformation behavior of the bilayer interface, the surface morphologies at sequential tensile strains

were characterized by SEM combined with a Kammrath-Weiss tensile tester. The 3D microstructures of the bilayer interface were observed by the micro-CT (Phoenix V tome x S240).

The layer thickness of the surface nanoscale SEBS layer of the bilayer interface was estimated by X-ray photoelectron spectroscopy (XPS) combined with CLSM observations. XPS measurements were performed with an X-ray Photoelectron Spectrometer (Thermo Fisher ESCALAB Xi+). Al Kα was used as the X-ray source (1486.7 eV), and the area for the analysis was 0.5 × 0.5 mm. The XPS depth profiling was performed by sputtering Ar ions. The ion energy is 2000 eV, the sputtering area is 5 × 5 mm, and the sputtering time for the first five and last six etching cycles are 30 s and 300 s. Fig. S5 shows the etching thickness as a function of etching time (cycle).

2.2 Electromechanical characterization

The electrical resistance was measured using a four-point probe with a digital source meter (Keithley 2601A). Electrical conductivity was calculated as $\kappa = l/Rwh$, where l, w, h and R are the length, width, conductive layer thickness, and resistance of the SEBS-LM composite, respectively. The conductive layer thicknesses were estimated by the cross-sectional SEM observations (Fig. S38). The samples were immersed directly in liquid nitrogen for 3 min and then cut into two halves for SEM observations. The electromechanical performances of both the bilayer interfaces and the soft-soft and soft-rigid connections were measured by a micro-force tensile testing machine (MTS® Tytron 250) coupled with a digital source meter at a constant strain rate of 1×10^{-2} s^{-1}. Three individual experiments were performed for each experimental condition. The samples used for electromechanical testing have a gauge section of 30 mm in length and 10 mm in width. The impedance spectra of the bilayer interface in Phosphate-Buffered Saline (PBS) solution in the frequency range of 10^{-1}-10^{5} Hz were collected on an electrochemical workstation (CS310M,

CORRTEST). Atomic force microscope (AFM) current mapping was generated using Bruker PeakForce TUNA mode (Bruker Dimension®Icon™).

2.3 Measurement of peeling force

The adhesion strength was measured by T-peel test (Fig. S23) with a micro-force tensile testing machine (MTS® Tytron 250) with a 50 N load cell. The T-type specimens were prepared by directly pressing an encapsulation layer (SEBS, PDMS, Ecoflex 30, PU, and VHB tape) on our bilayer interface. The T-type specimens have a length of 50 mm and a width of 10 mm. The bonding region has a length of 30 mm and a width of 10 mm. Each bonded specimen was clamped with the grips and loading was applied (Fig. S23a). The peel tests were conducted at a displacement rate of 10 mm min^{-1}. In each test, the load-displacement curve was recorded. The adhesion strength is the peel force per unit width required to separate the bilayer interface and encapsulation layer, which was taken from the plateau region (Fig. S23b) of the force - displacement curve after the initial peak reading. Three individual experiments were performed for each type of sample.

3. In vivo and in vitro experiments

All in vivo experiments were performed in Xi'an Jiaotong University, which was approved by the Institutional Animal Care and Use Committee (IACUC) of Xi'an Jiaotong University, and the approval number is 2019-773. Adult Sprague-Dawley rats 3 months in age (~ 250 g) were anesthetized by injecting sodium pentobarbitone (density 2%, dose 0.3 ml per 100 g) into the intraperitoneal space, and checked for the depth of anesthesia. All samples were prepared in an aseptic manner and were further disinfected under ultraviolet light for 3 h.

3.1 Stimulation of peroneal nerve and recording of EMG signals from the peroneus longus muscle.

After shaving, the vastus lateralis muscle and biceps femoris muscle were dissected to expose

the peroneal nerve and peroneus longus muscle, and the area was irrigated with sterile saline to ensure a clear view and good electrical contact. In the simultaneous stimulation and recording experiment, we used the bilayer electrode to stimulate the peroneal nerve and recorded the EMG signals generated by the gastrocnemius muscle, because the bilayer electrode is self-adhesive, no suturing is required. The bilayer electrode was first inserted under the nerve or muscle, then folded over and pressed to secure the electrode. The stimulus pulses were applied and EMG signals were recorded using the Acquisition System of Electrophysiological Signals (BL-422L, TECHMAN). Measurement of EMG signals in the vibration state by placing rats on a vibrator. The stimulation pulse was applied using an electrical stimulator (monophasic pulse, width 200 μs, frequency 1 Hz).

3.2 In vitro cell experiments

The electrodes and cell slides were placed in 24-well plates and each well was seeded with 3×10^4 cells contained in 500 μL culture medium; the culture medium was refreshed every two days. Live/Dead Viability/Cytotoxicity Kit (Molecular Probes, Invitrogen) was used to identify viable and dead bone mesenchymal stem cells (BMSCs) on the different samples after 3 days of incubation. Specifically, the cell-adhered samples were washed twice using PBS followed by the addition of 300 μL PBS containing ethidium-homodimer-1 (dilution of 1:2000) and calcein-AM (dilution of 1:4000) to each well prior to incubating at 37 °C for 30 min. The fluorescence-stained cells were analyzed using laser confocal microscope (FV1200, Olympus) for the collection of images of live/dead cells on samples. Four specimens from each group were tested, and each test was repeated three times.

3.3 Animal experiments

Adult Sprague-Dawley rats 3 months in age (~ 250 g) were used for evaluate the biocompatibility of the electrodes (n = 6 for each group). Veterinary Drug (031217015) 2.0% ~ 2.5%

isoflurane mixed with oxygen was used to induce anesthesia for 5 min using a small animal anesthesia machine (RWD, R583S). Under sterile conditions, three dorsal skin incisions were made, one of the incisions was sutured directly (sham operation group), bilayer electrode and Ag-SEBS electrodes were implanted in the other two incisions, respectively. After that, muscle, subcutaneous tissue, and skin were sutured and the rats were housed in separate cages and allowed to move freely in the cages. After 7 days and 14 days, the blood samples (0.5 mL) were procured from tail vein, respectively, and transferred to EDTAK2 test tube which was used for blood routine test.

4. Human electrocardiogram (ECG) signal recording

For the ECG signal recording, a wearable ECG signaling wristband can be made by joining the bilayer electrodes and thin SEBS sheets using soft-soft connections. Two wearable wristbands were wrapped around the wrists of the left and right arms of a volunteer (Fig. S36). Another bilayer electrode was attached on the left ankle as a reference electrode. All the electrodes were connected to a physiological signal acquisition system (RM6240EC, CHENGDU INSTRUMENT FACTORY) for the acquisition of ECG signals.

For the long-term ECG signal recording, the bilayer electrode and commercial Ag/AgCl electrode were adhered to the skin throughout the duration of the recordings, while normal activities such as working and exercise were conducted as usual.

5. Calculation of signal-to-noise ratio (SNR)

The SNR can be calculated by the following equation:

$$SNR(\mathrm{dB}) = 20\lg\frac{A_{signal}}{A_{noise}} \tag{S1}$$

where A_{signal} is the amplitude of the signal, and A_{noise} is the amplitude of noise. The SNR was

calculated from over 50 of PQRST waveforms in each ECG signal.

6. Supplementary information notes

Note S1: Analysis on settlement of LM particles

The LM particles inside SEBS solution are subjected to gravity, buoyancy, and drag force (the latter occurs only if the particles are moving) (Fig. S28). LM particles were naturally settled towards the bottom of the SEBS matrix due to the large density of LM. Assuming the LM particles are spherical, the gravitational force (F_g) on LM particles can be expressed as:

$$F_g = \frac{4\pi r^3}{3}\rho_{LM} g \quad \text{(S2)},$$

where ρ_{LM} is the density of the LM, r is the radius of the LM particle, and g is the gravitational acceleration.

The buoyancy force (F_b) on LM particles is given by:

$$F_b = \frac{4\pi r^3}{3}\rho_{SEBS} g \quad \text{(S3)},$$

where ρ_{SEBS} is the density of the SEBS.

The drag force (F_d) on LM particles is induced by the viscosity of the SEBS solution, which can be calculated by the Stokes formula[1]:

$$F_d = 6\pi\mu r v \quad \text{(S4)},$$

where μ is the viscosity of the SEBS solution, and v is the velocity of the LM particles relative to the SEBS.

Equation S5 expresses a steady state balance among gravity, buoyancy, and drag on the LM particles in SEBS, which is given by:

$$\frac{4\pi r^3}{3}\rho_{LM} g - 6\pi\mu r v - \frac{4\pi r^3}{3}\rho_{SEBS} g = 0 \quad \text{(S5)}$$

According to the Stokes' flow settling, the velocity of LM particles inside SEBS solution can be expressed as:

$$v = \frac{2(\rho_{LM} - \rho_{SEBS})}{9\mu} r^2 g \quad \text{(S6).}$$

Thus, v scales with r^2. We measured the viscosity of the SEBS solution (13 wt.%, toluene) using a rotational viscometer (IKA ROTAVISC hi-vi). Taking μ = 15000 cP for SEBS solution, ρ_{SEBS} = 0.83 g cm^{-3}, and ρ_{LM} = 6.25 g cm^{-3}, the sedimentation velocities v are calculated to be 4.9 × 10^{-1} μm s^{-1} for r = 25 μm, 1.2 × 10^{-1} μm s^{-1} for r = 12.5 μm and 4.4 × 10^{-4} μm s^{-1} for r = 0.75 μm.

As the LM particles move towards the bottom, they impact other LM particles at the bottom. We assume that all the forces on the particles act in the vertical direction, and the terminal velocity of LM particle is zero. According to the impulse momentum theorem, the impact force (F_i) between the two LM particles can be expressed as:

$$F_i = \rho_{LM} \frac{4\pi r^3 v}{3t} \quad \text{(S7),}$$

where t is the duration of the collision.

The pressure acts on the LM particle can be calculated by:

$$P = \frac{F_i}{A} \quad \text{(S8),}$$

where A is the contact area during the collision.

We estimated experimentally the duration of the collision and the contact area A between two LM particles. As shown in Fig. S29, a LM particle with a diameter of 1.6 mm was dropped from a height of 1 mm with the help of a syringe and impacted on a 500 μm-thick LM coating surface. The particle impacting process was recorded using a high-speed camera. The duration of the collision t is estimated to be ~ 78 ms and the contact area A is approximately one-half of the total surface area of the spherical particle (Fig. S29).

Substituting ρ_{LM}=6.25 g cm^{-3}, g=9.8 m s^{-2}, t = 78 ms, v=4.9 × 10^{-1} μm s^{-1}, 1.2 × 10^{-1} μm s^{-1}, and

4.4 × 10^{-4} μm s^{-1} into the equation S8, the pressure P is calculated to be 6.54×10^{-7} MPa, 8.01×10^{-8} MPa, and 1.76×10^{-11} MPa for r = 25 μm, 12.5 μm, and 0.75 μm, respectively.

It is found that the critical stress for rupturing oxidation layer of LM particles is inversely proportional to the particle radius [2]:

$$P_c = \frac{6.16d + 3.04\times10^{-7}}{\pi d^2} \quad \text{(S9)}.$$

The critical rupture stress P_c is calculated to be ~ 3.93×10^{-2}, 7.86×10^{-2} and 1.35 MPa for r = 25 μm, 12.5 μm, and 0.75 μm, respectively. A comparison indicates that the pressure P is considerably smaller than the P_c.

Even assuming t =10 μs [3], the pressure P is only 5.10×10^{-3} MPa, 6.25×10^{-4} MPa, and 1.38×10^{-7} MPa for r = 25 μm, 12.5 μm, and 0.75 μm, respectively, still much smaller than the P_c.

Additionally, if assuming that the contact area A is one ten thousandth of the total surface area of the spherical particle, the pressure P is calculated to be 3.27×10^{-3} MPa, 4.01×10^{-4} MPa, and 8.81×10^{-8} MPa for r = 25 μm, 12.5 μm, and 0.75 μm, respectively, which also are significantly smaller than the P_c.

Therefore, the impact force induced by gravity is insufficient to rupture the oxide layer for achieving self-sintering.

Note S2: Analysis on the capillary force induced by solvent evaporation

As sketched in Fig. S30a, the capillary force (F_c) induced by the liquid bridge between LM particles acts on the LM particles. The capillary force during solvent evaporation originates from the surface tension and the Laplace pressure, which can be expressed as[4]:

$$F_c = 2\pi\gamma r \sin\varphi \sin(\varphi+\theta) + \pi r^2 \sin^2\varphi \Delta P \quad \text{(S10)},$$

where γ is the surface tension of the liquid, r is the LM particles radius, φ is the half-filling angle, θ is the liquid-solid contact angle, and ΔP is the pressure difference cross the liquid surfaces, which is given by:

$$\Delta P = \frac{2\gamma\cos\theta}{r_p} \quad \text{(S11)},$$

where r_p is the capillary curvature radius.

The capillary forces could also be represented as[5]:

$$F_c = 2\pi\gamma r \sin\varphi \sin(\varphi+\theta) + 2\pi\gamma r \cos\theta/(1+H/2a) \quad \text{(S12)},$$

where H is the shortest distance between the spheres, a is the immersion length of the sphere ($a = (H/2)\times[-1+\sqrt{1+2V/\pi rH^2}]$)[5], where V is the volume of liquid bridge).

The pressure difference crosses the liquid surfaces can be calculated by [6]:

$$P = F_c/\pi[r^2-(r-a)^2] \quad \text{(S13)}$$

We estimated experimentally the half-filling angle φ and liquid-solid contact angle θ (Fig. S30b). Two LM particles (1.8 mm in diameter) were dropped on a glass plate by a syringe. A toluene droplet (0.1 ml) was added between the two LM particles. The corresponding configurations were imaged with a high-speed camera. Here, we assume H = 500 nm and V = 10^9 nm^3 for r = 25 μm, H = 250 nm and V = 10^8 nm^3 for r = 12.5 μm, and H = 50 nm and V = 10^6 nm^3 for r = 0.75 μm, respectively. Taking $\gamma_{Toluene}$ = 29 mN m^{-1}, φ = ~ 40° and θ = ~ 7°, the pressure P acting on the LM

particles is calculated to be 1.21 MPa, 2.95 MPa, and 4.47 MPa for r = 25 μm, 12.5 μm, and 0.75 μm, respectively.

Obviously, the pressure P are generally greater than the critical rupture stress (3.93×10^{-2} MPa for r = 25 μm, 7.86×10^{-2} MPa for r = 12.5 μm and 1.35 MPa for r = 0.75 μm). Thus, the capillary force generated during the solvent evaporation are large enough to rupture the oxidation layers of LM particles, triggering the self-sintering of LM particles.

Note S3: Analysis on the effect of the nanoscale SEBS layer on the electrical resistance

The thickness of the nanoscale SEBS layer can be tuned by changing the LM particle size and the weight ratio of toluene to SEBS in solution.

We have investigated the effect of size of LM particles on the thickness of the SEBS layer. We prepared the bilayer interfaces with the same LM volume fraction (30%) but different LM particle sizes (diameters, d) of 50, 25, and 1.5 μm. XPS depth profiling analysis was performed to determine the thickness of the ultrathin SEBS layer. Following the same procedures, the thicknesses of surface SEBS layers were estimated to be ~ 40 nm for d = 50 μm, ~ 37 nm for d = 25 μm, and ~ 24 nm for d = 1.5 μm, respectively.

We have measured the electromechanical responses of bilayer electrodes with different thicknesses of surface SEBS layers. As shown in Fig. S39, the initial resistance decreases with increasing (decreasing) particle diameter (SEBS layer thickness). It was expected that the thinner SEBS layer induces the lower resistance, which is inconsistent with the experiments. This means that the electrical resistance is mainly affected by the conductive network of LM particles when the surface SEBS layer has a thickness of $\leqslant$ 40 nm. According to quantitative analysis of the capillary force induced by solvent evaporation (Note S2), for average diameters of LM particles ranging from 1.5 to 50 μm, the capillary forces are large enough to rupture the oxide shells. The released LM could flow out and coalesce into a conductive network, resulting in self-sintering. It is noteworthy that the capillary pressure is much larger than the rupture stress for larger LM particles, while the capillary pressure is slightly larger than the rupture stress for smaller LM particles. Considering wide distribution of LM particle size, more conductive pathways tend to form in SEBS-LM composites with larger LM particles, leading to lower electrical resistance. Thus, the initial resistance decreases with increasing particle diameter.

We also investigated the effect of the weight ratio of toluene to SEBS on the surface SEBS layer thickness. We prepared bilayer interfaces with same d and different surface layer thicknesses by adjusting the weight ratio (ω) of toluene to SEBS. The SEBS layer thicknesses were estimated to be ~ 35 nm for ω = 10%, ~ 40 nm for ω = 13%, and ~ 44 nm for ω = 17%, respectively. As shown in Fig. S40, the initial resistance slightly decreases with decreasing layer thickness due to the small tunneling distance.

7. Supplementary information figures

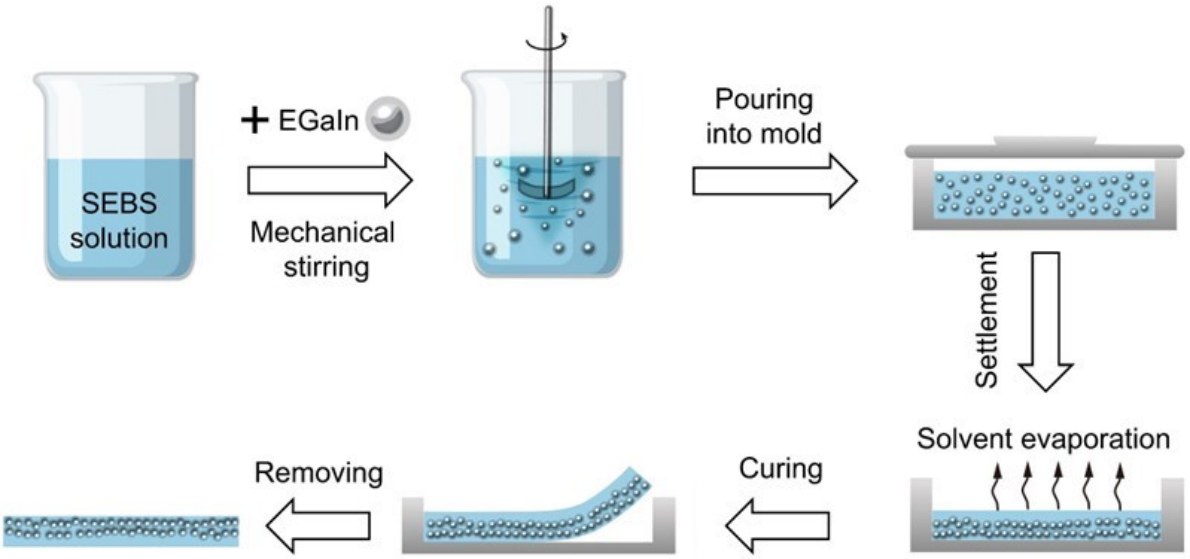

Figure S1. Schematics of fabrication process of the stretchable, conductive and adhesive bilayer interface.

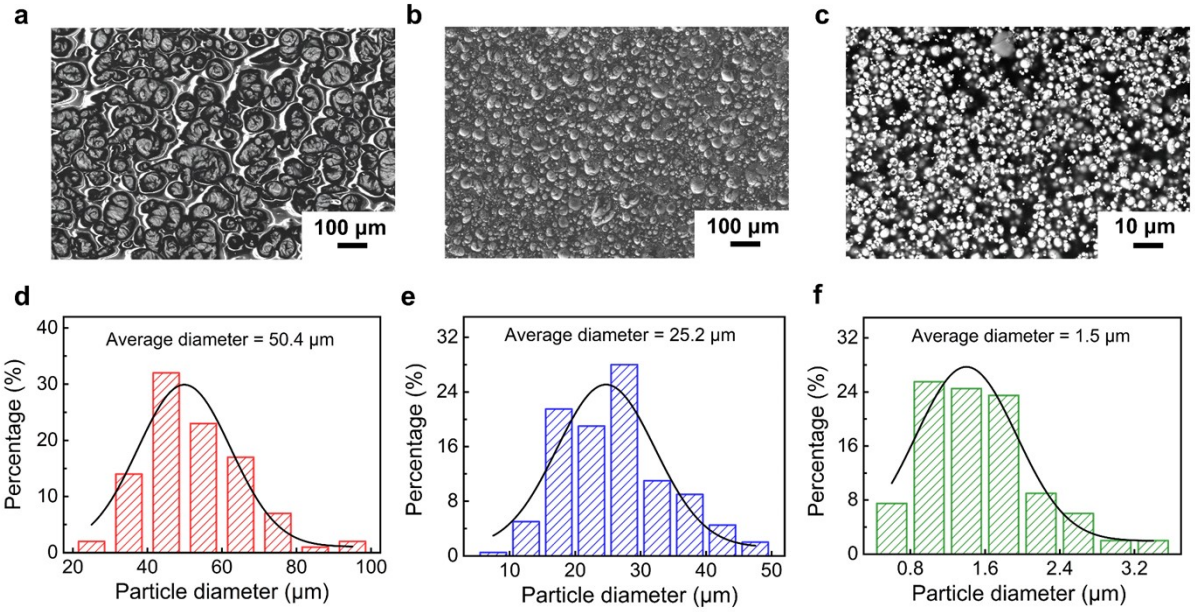

Figure S2. SEM images of the bilayer interfaces with (a) d = 50.4 μm, (b) d = 25.2 μm, and (c) d = 1.5 μm. Size distributions of LM particles in the bilayer interfaces with (d) d = 50.4 μm, (e) d = 25.2 μm, and (f) d = 1.5 μm. The polydispersity of the LM particles may also improve the packing density, i.e., small particles could fill the gaps between large particles, facilitating the formation of conductive pathway during sedimentation.

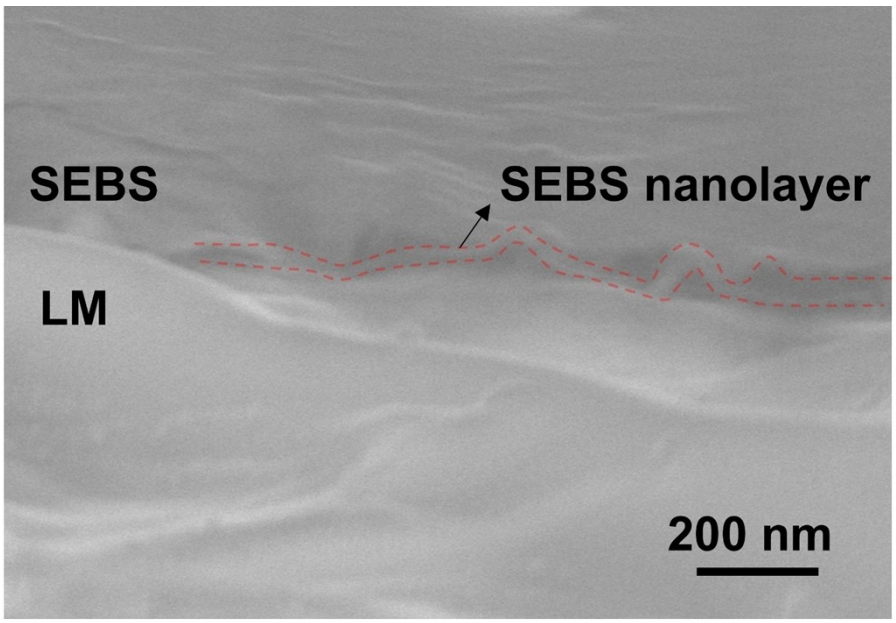

Figure S3. Cross-sectional SEM image of the nanoscale SEBS layer on the surface of the bilayer interface. The samples were immersed directly in liquid nitrogen for 3 min and then cut into two halves for SEM observations. The ultrathin SEBS layer with an average thickness of ~ 38 nm can be detected from the cross-sectional SEM image. This is in general agreement with the results of XPS depth profiling analysis.

1 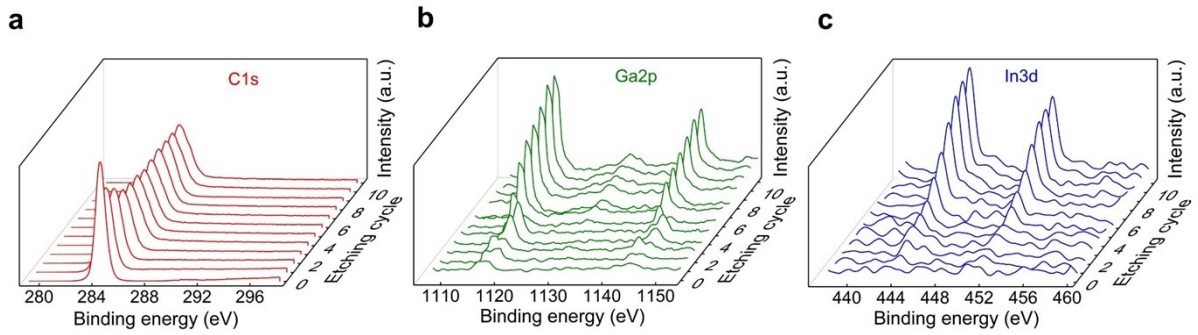

2 **Figure S4.** Evolution of XPS spectra of (a) C 1s, (b) Ga 2p, and (c) In 3d with etching cycles**.**

3

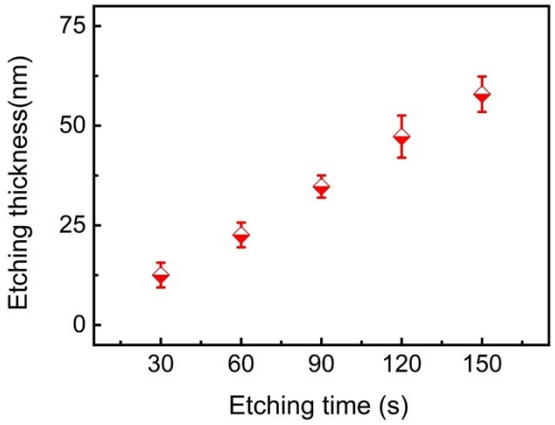

Figure S5. Variation of etching thickness with etching time.

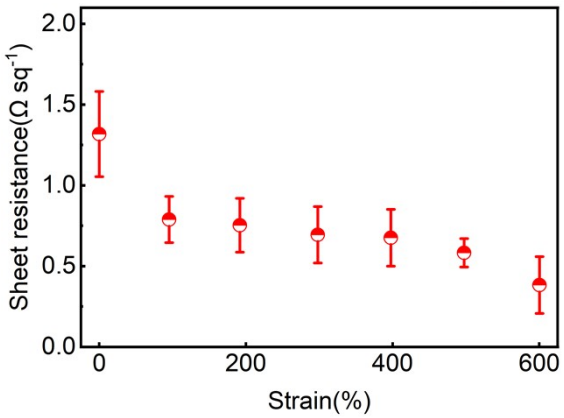

Figure S6. Evolution of sheet resistance of the bilayer electrode with tensile strain from 0 to 600% strain. The surface nanoscale SEBS layer has a thickness ≤ ~ 40 nm, which is thin enough for electron tunneling through the top ultrathin SEBS layer to form out-of-plane conductive pathway with underlying SEBS-LM composite layer under an applied voltage of 3 V (Similar electron tunneling effects occur in various polymers under certain applied voltage,[7-12] such as PDMS with thicknesses of even larger than 400 nm under a voltage of 0.5-10 V.[7, 9]).

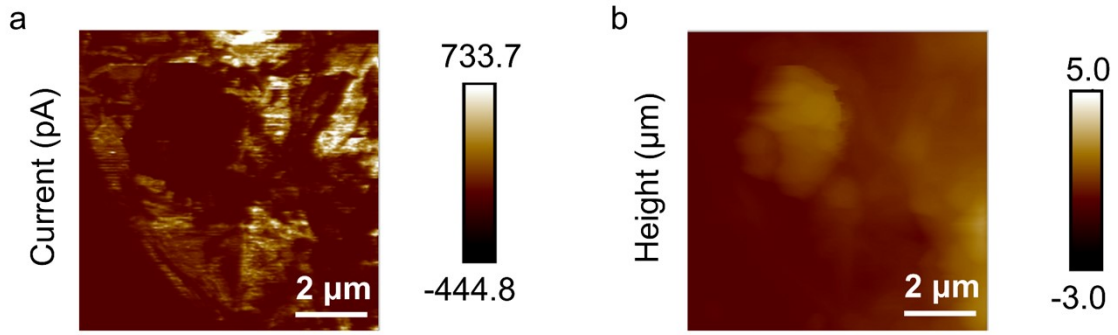

Figure S7. (a) AFM current mapping and (b) AFM height mapping of the bilayer interface. The uniformity of current intensity distribution originates from the fluctuations in the thickness of nanoscale SEBS layer and the surface topography.

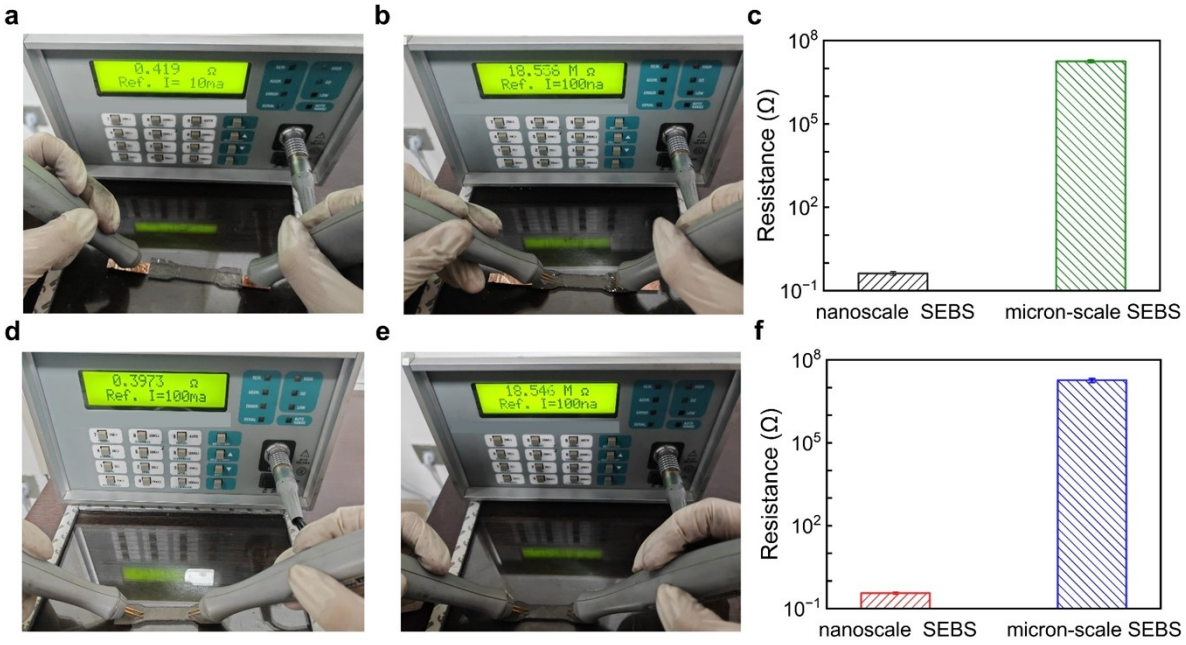

Figure S8. Photographs of resistance measurements on the (a) front (nanoscale SEBS/SEBS-LM composite layer) and (b) back (micron-scale SEBS layer) of the trilayer sample before removal from the mold. (c) Resistance values measured from the front and back of the trilayer sample before removal from the mold. Photographs of resistance measurements on the (d) front (nanoscale SEBS/SEBS-LM composite layer) and (e) back (micron-scale SEBS layer) of the trilayer sample after removal from the mold. (f) Resistance values measured from the front and back of the trilayer sample after removal from the mold.

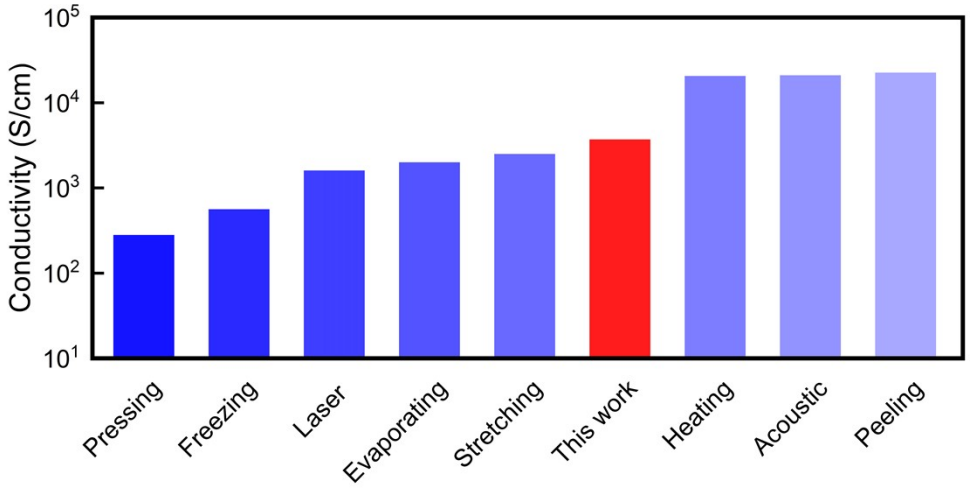

Figure S9. Comparison of initial conductivity of our self-sintering bilayer interface with polymer-LM -based conductors by different sintering processes, including pressing[13], freezing[14], laser[15], evaporating[6], stretching[16], heating[17], acoustic[18], peeling[19].

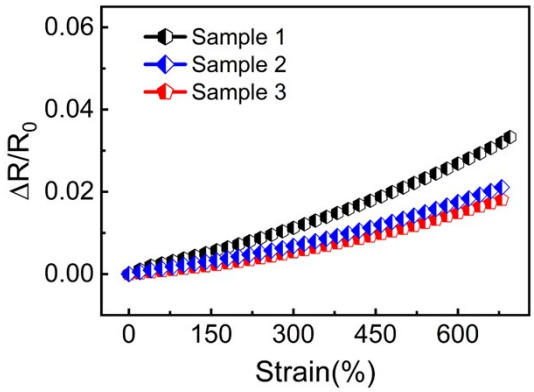

Figure S10. Electromechanical responses for three bilayer interface samples fabricated under the same condition.

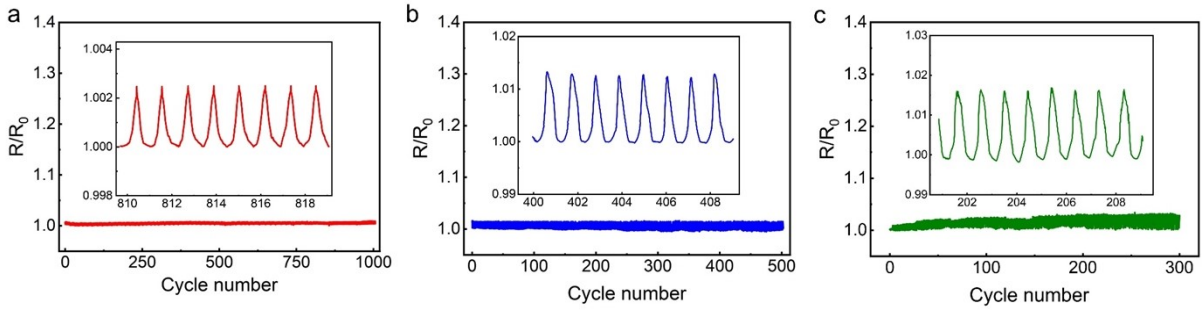

Figure S11. Resistance changes versus cycle number (a) at 100% strain for 1000 cycles, (b) at 300% strain for 500 cycles and (c) at 500% strain for 300 cycles. Note that the electrical resistance decreases in the first few stretching/releasing cycles, because some intact LM particles rupture and coalesce under deformation, which induces an increase in effective conductive pathway. Thus, the resistance changes of bilayer interfaces in cyclic tests were measured after they reached stable status.

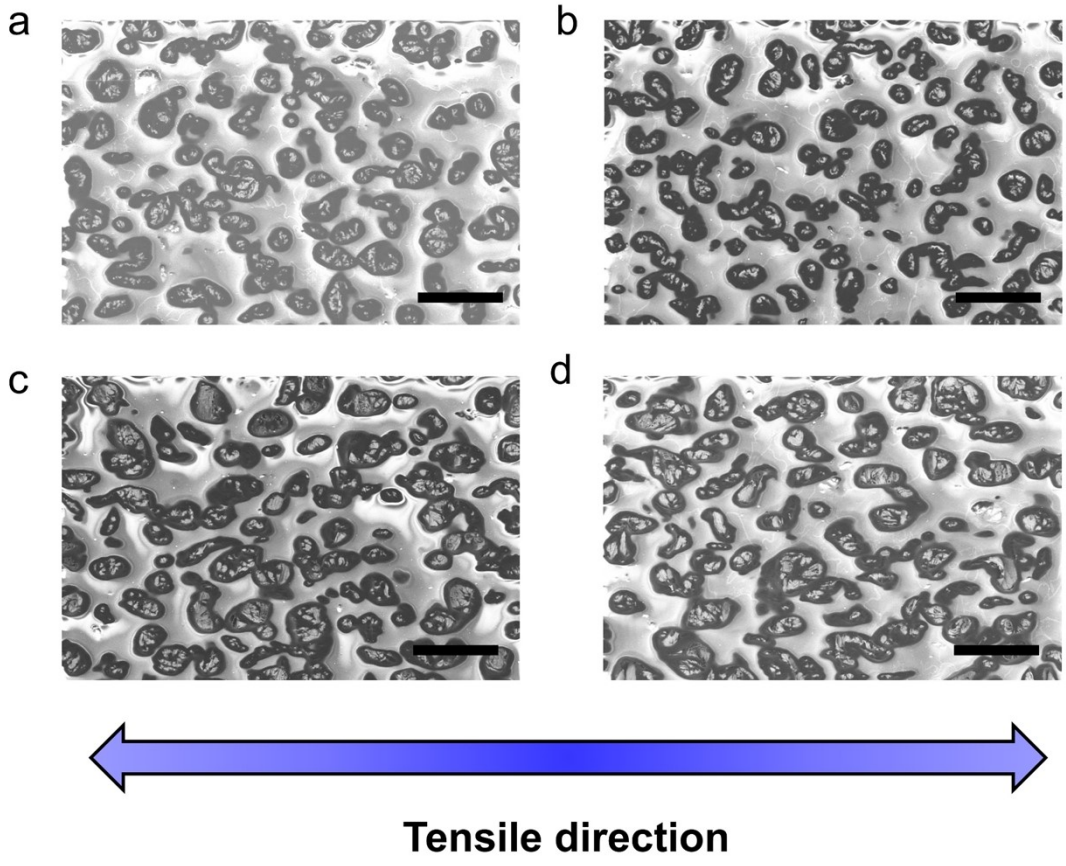

Figure S12. (a) SEM image of the bilayer interface before stretching. (b) SEM image of the bilayer interface after 1000 cycles at 100% strain. (c) SEM image of the bilayer interface after 500 cycles at 300% strain. (d) SEM image of the bilayer interface after 300 cycles at 500% strain. (Scale bar, 200 μm). The LM particles change from a round to an elliptical shape after 300 cycles at 500% strain due to the viscoelastic behaviour of SEBS.

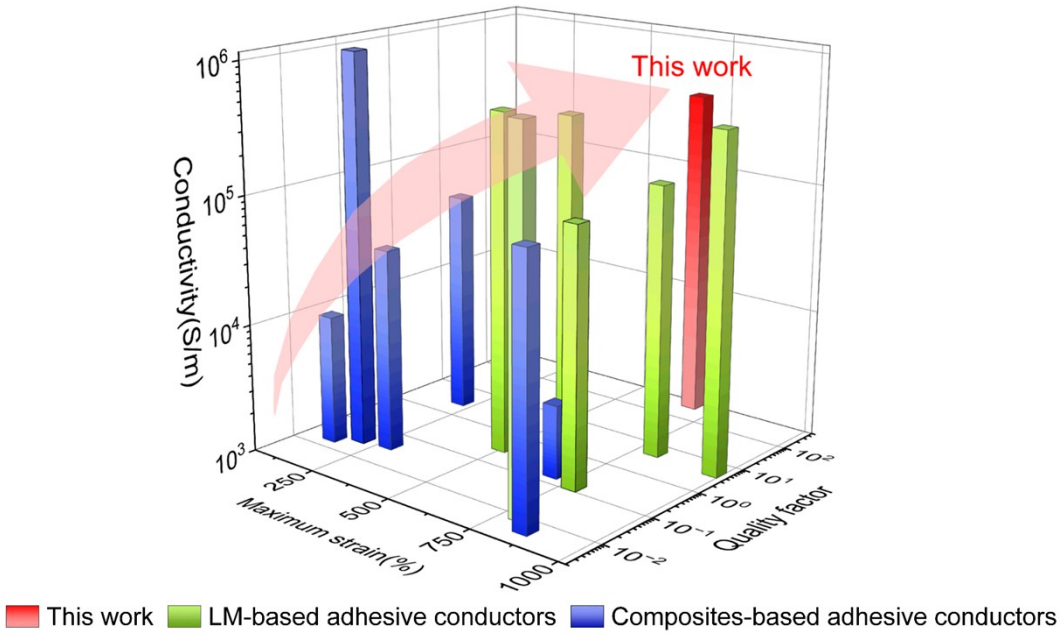

Figure S13. Comparisons of the conductivity, quality factor Q, and maximum strain of our bilayer interface with reported stretchable and adhesive conductors for electrical interfacing, including LM-based adhesive conductors[20-25] and composites-based adhesive conductor consisting of polymer or hydrogel with conductive fillers.[26-31]

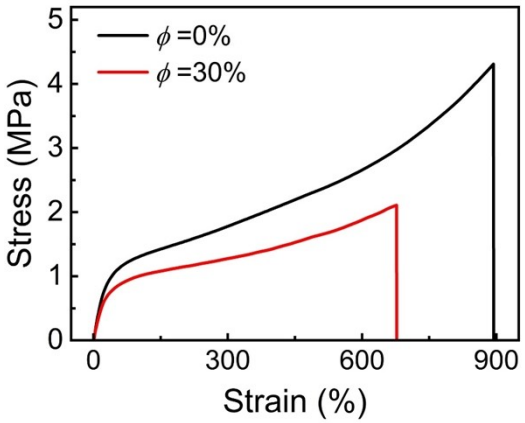

Figure S14. Stress-strain curves of the pure SEBS and the trilayer sample with ϕ = 30% under tension. A sudden drop in force is caused by the complete fracture of the specimens.

1 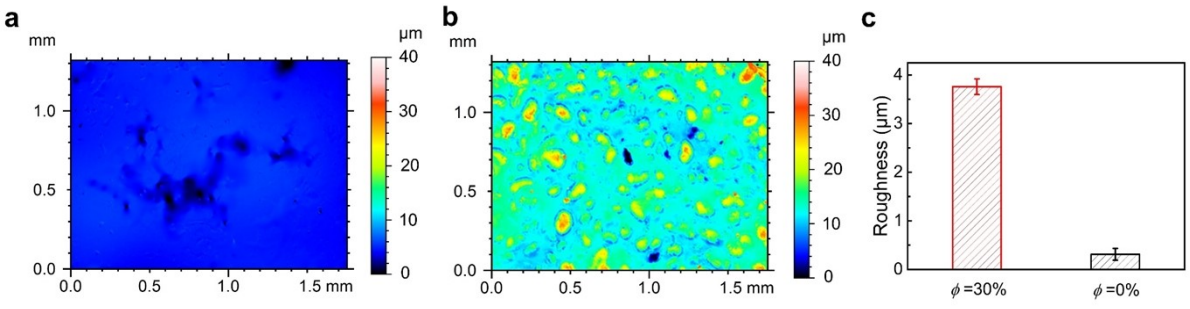

2 **Figure S15.** Two-dimensional CLSM images of a) pure SEBS and b) bilayer interface with ϕ = 30%.

3 c) Surface roughness of pure SEBS and bilayer interface with ϕ = 30%.

4

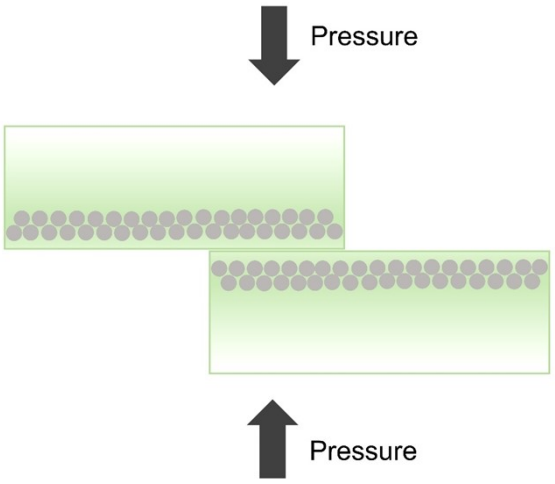

Figure S16. Schematic of fabrication process of the soft-soft connection using the bilayer interface.

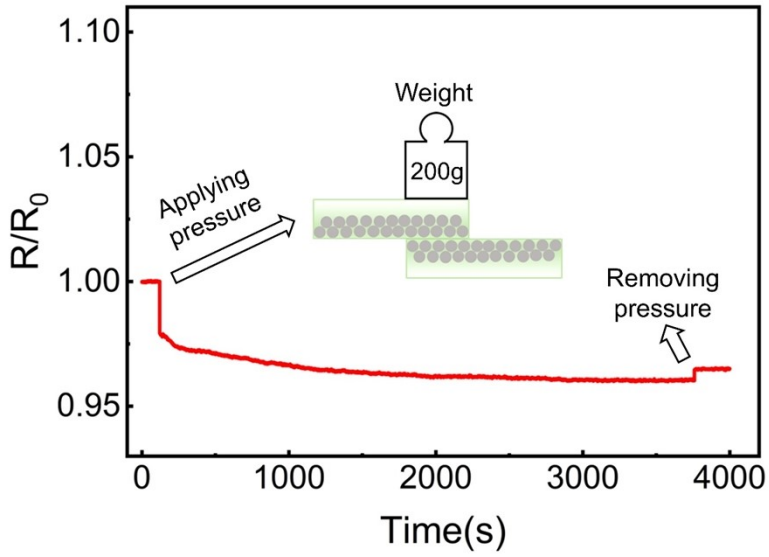

Figure S17. Resistance changes during applying and removing pressure for soft-soft connections. The resistance decreases only 4% when a 200 g weight was applied on the bonding region. The resistance remains almost unchanged during loading for one hour. Upon unloading, the resistance increases slightly, which is only 3% lower than the initial resistance value.

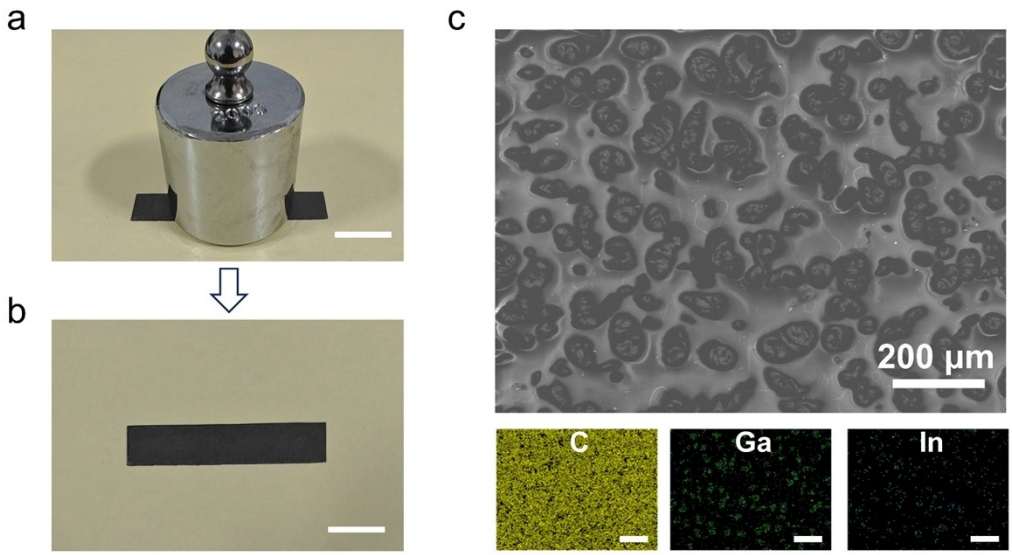

Figure S18. (a) Digital image of the bilayer interface when pressure was applied. (b) Digital image of the bilayer interface after applying pressure. (c) SEM images with corresponding EDS analysis of the bilayer interface after applying pressure.

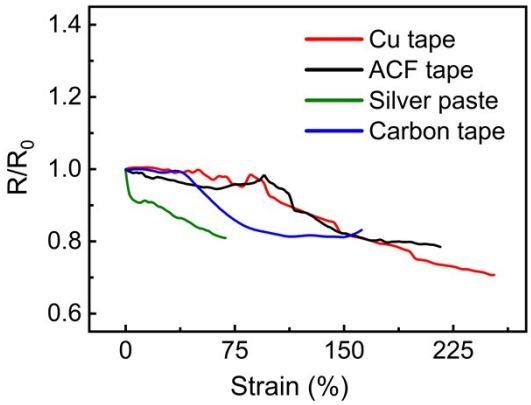

Figure S19. Relative resistance changes as a function of strain for soft-soft (bilayer interface-bilayer interface) connections using different commercial pastes.

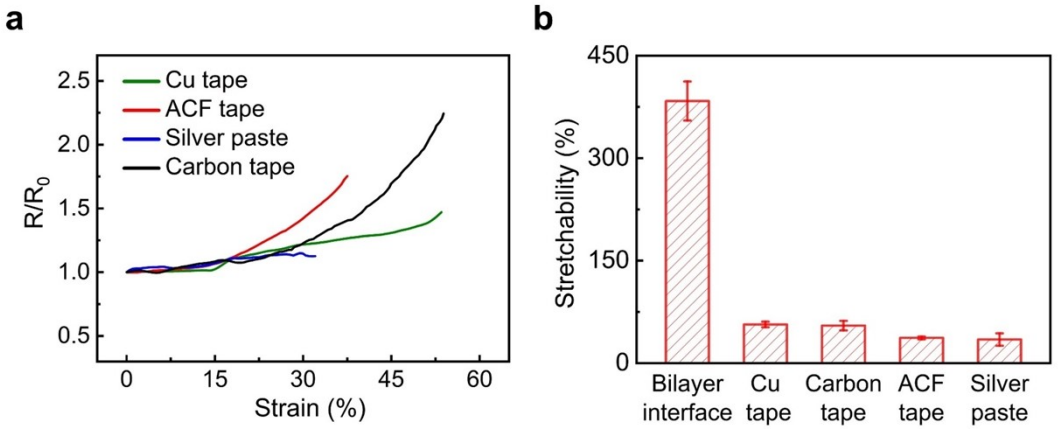

Figure S20. (a) Relative resistance changes as a function of strain for conventional soft-soft (PDMS-LM/PDMS-LM) connections using different commercial pastes. (b) Comparison of the stretchability of soft-soft connections, including bilayer interface-bilayer interface connection, and PDMS-LM/PDMS-LM connections using different commercial pastes.

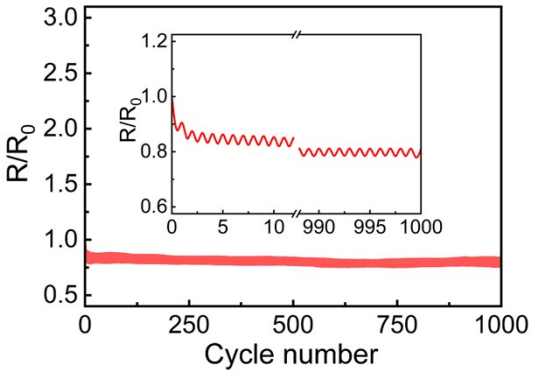

Figure S21. Resistance changes of the soft-soft connections using the bilayer interface versus cycle number at 100% strain.

1 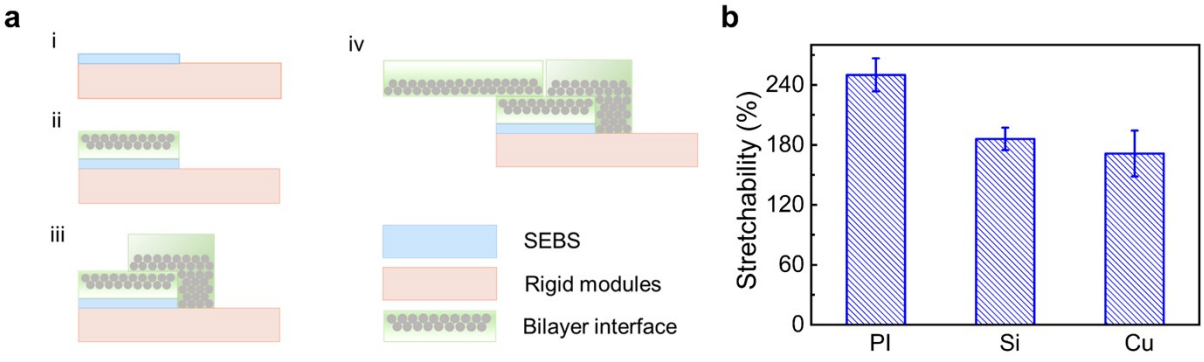

2 **Figure S22.** (a) Schematic of fabrication process of the soft-rigid connection using the bilayer
3 interface. (b) Comparison of the stretchability of soft-rigid connections using the bilayer interface on
4 different substrates, including polyimide (PI), silicon (Si), and copper (Cu).

5

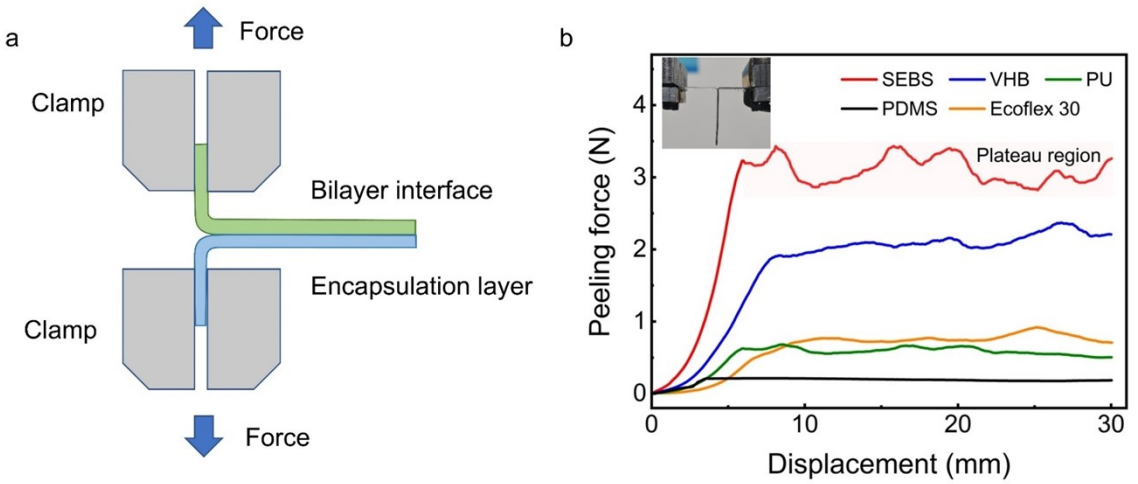

Figure S23. (a) Schematic of the experimental setup of T-peel test. (b) Force-displacement curves of the T-type samples with different encapsulation layers (SEBS, PDMS, Ecoflex 00-30, PU, and VHB tape)**.**

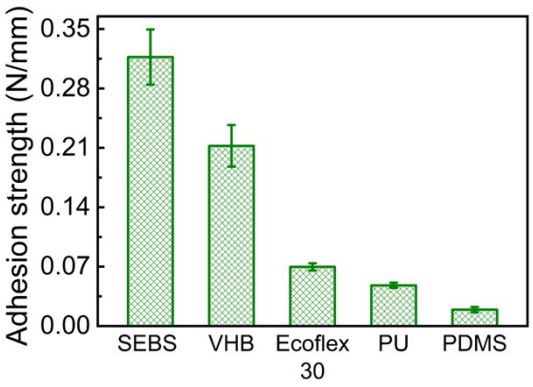

1

2 **Figure S24**. Adhesion strength of soft-encapsulation connections between the bilayer interfaces and

3 different encapsulations, including SEBS, PDMS, VHB tape, PU, and Ecoflex.

4

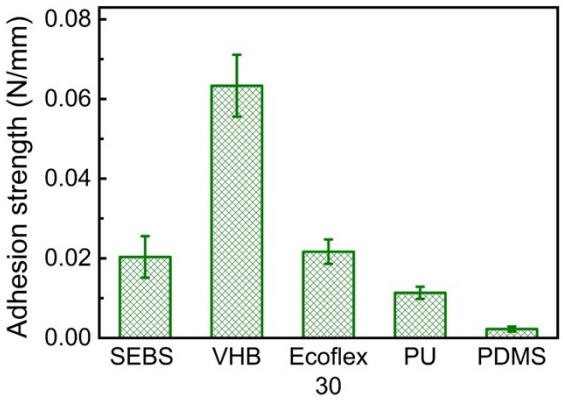

Figure S25. Adhesion strength of the conventional encapsulation connections between PDMS-LM composite and different encapsulation layers, including SEBS, PDMS, VHB tape, PU, and Ecoflex.

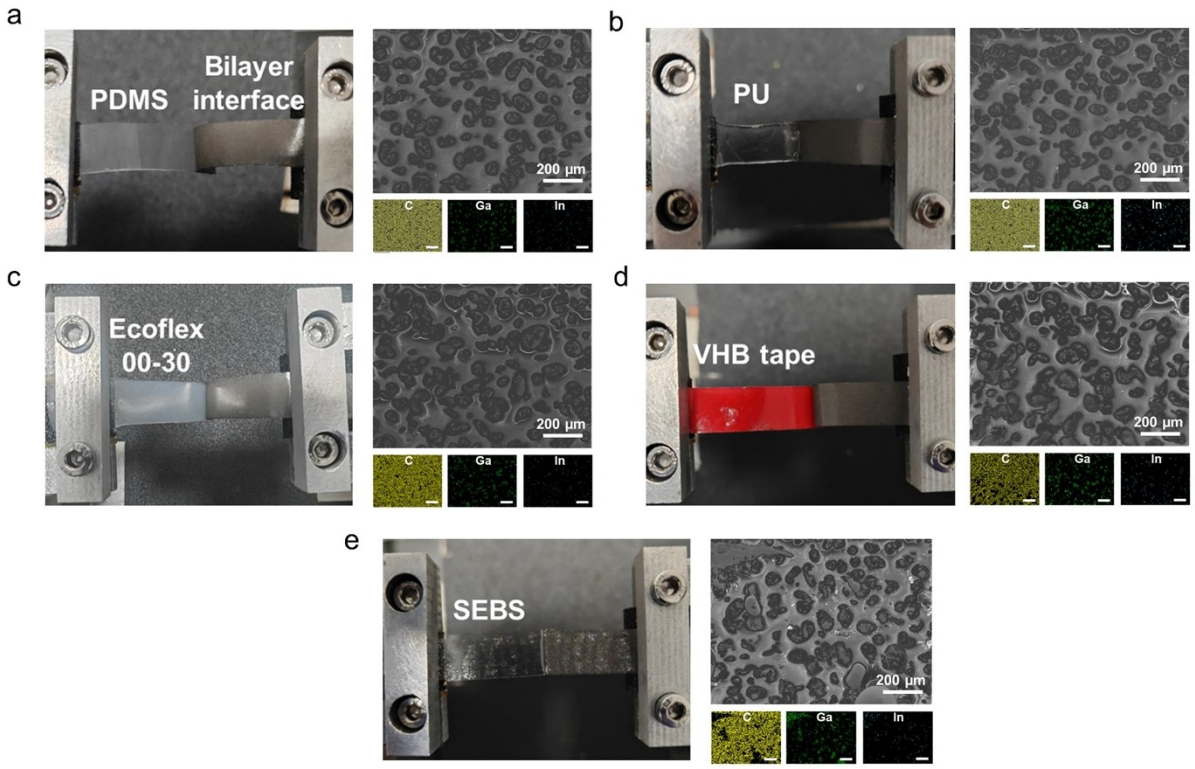

Figure S26. Digital images of the peeling process between the bilayer interface and different encapsulation layers and SEM images with corresponding EDS analysis after peeling of the bilayer interface. (a) PDMS and bilayer interface. (b) PU and bilayer interface. (c) Ecoflex 00-30 and bilayer interface. (d) VHB tape and bilayer interface. (e) SEBS and bilayer interface.

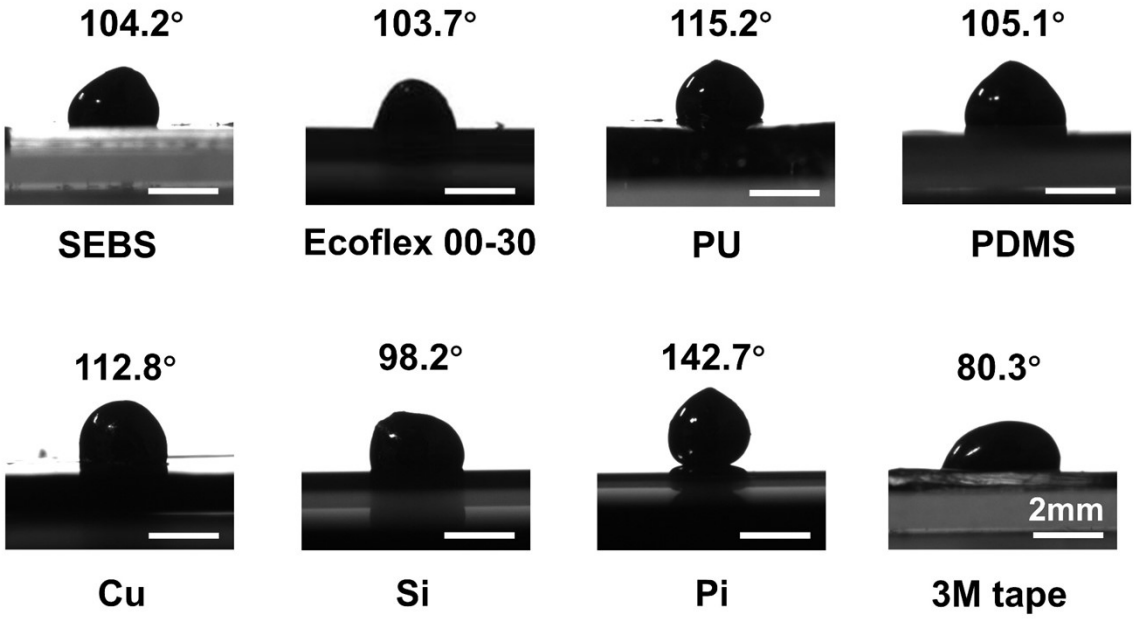

Figure S27. Contact angles of LM droplets on various substrates, including SEBS, Ecoflex 00-30, PU, PDMS, PI, copper, silicon, and VHB tape. All contact angles are larger than 90° except for the VHB tape. Although the contact angle between LM and VHB tape is less than 90°, the SEBS nanolayer prevents their direct contact. Therefore, the adhesion of the bilayer electrode is not affected by LM droplets. The bilayer interface has strong adhesion with dissimilar modules, which is attributed to the nanoscale self-adhesive SEBS layer.

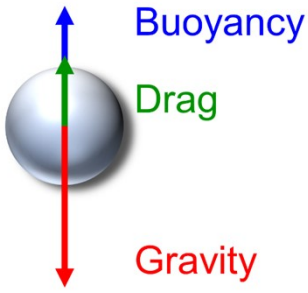

Figure S28. Schematic of gravity, buoyancy and drag forces acting on LM particles in SEBS solution.

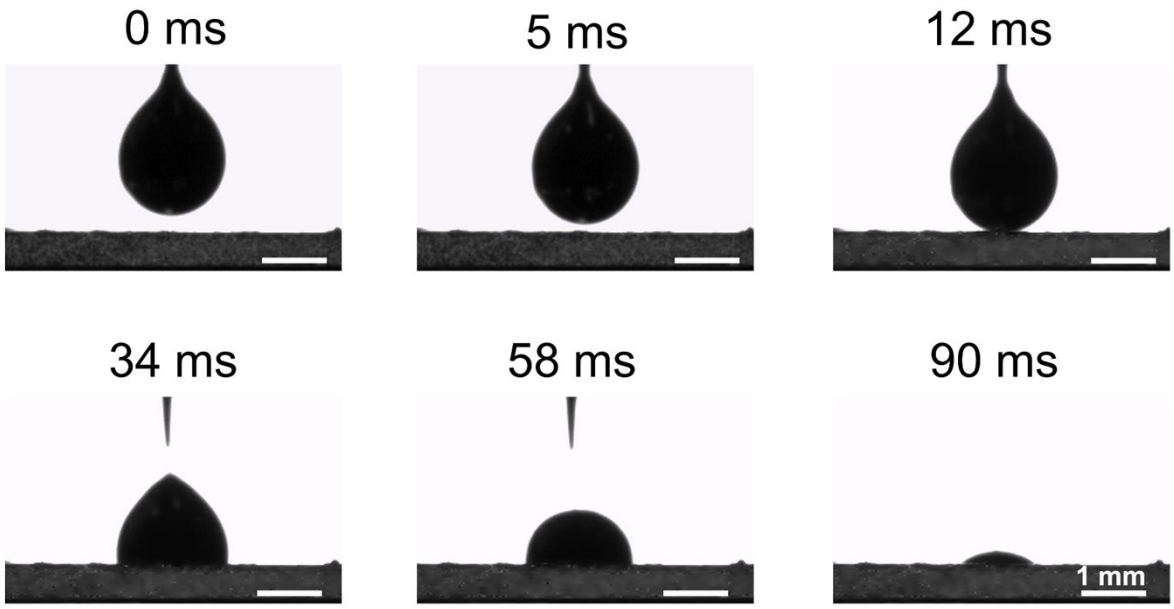

Figure S29. Serial images of snapshots of a LM particle impact on LM coating. The duration of the collision is defined as the time difference between the beginning of collision of the LM particle with the LM coating (12 ms) and the flattening of the LM particle (90 ms). During the whole collision process, the average contact area A is estimated to be approximately one-half of the total surface area of the spherical particle.

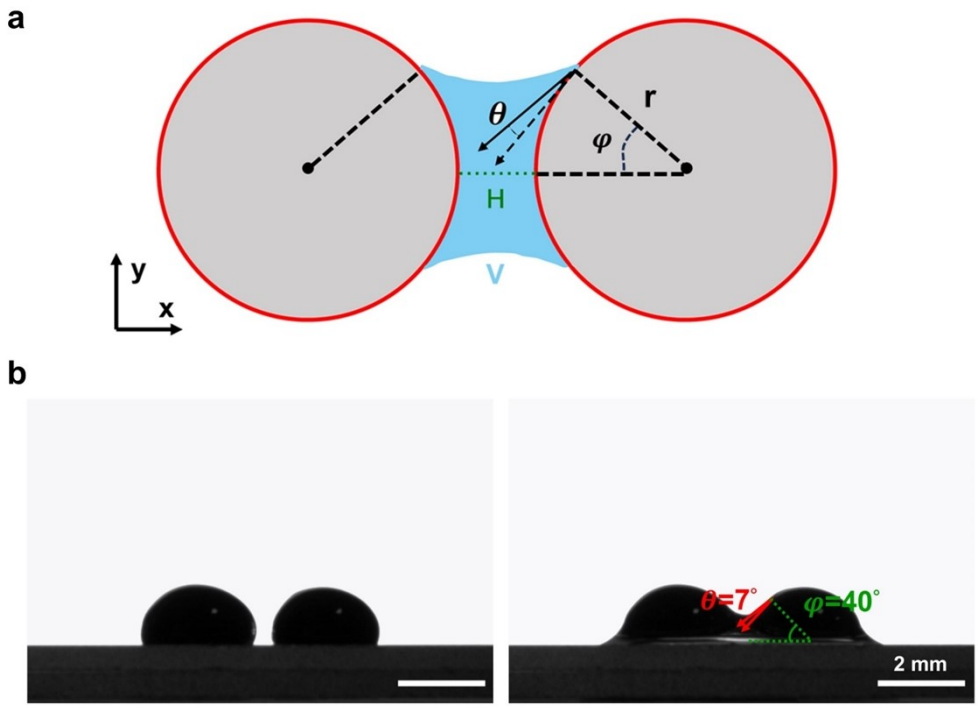

Figure S30. (a) Schematic of capillary force between two LM particles. (b) Photographs of the estimation of solid-liquid contact angle θ and half-filling angle φ.

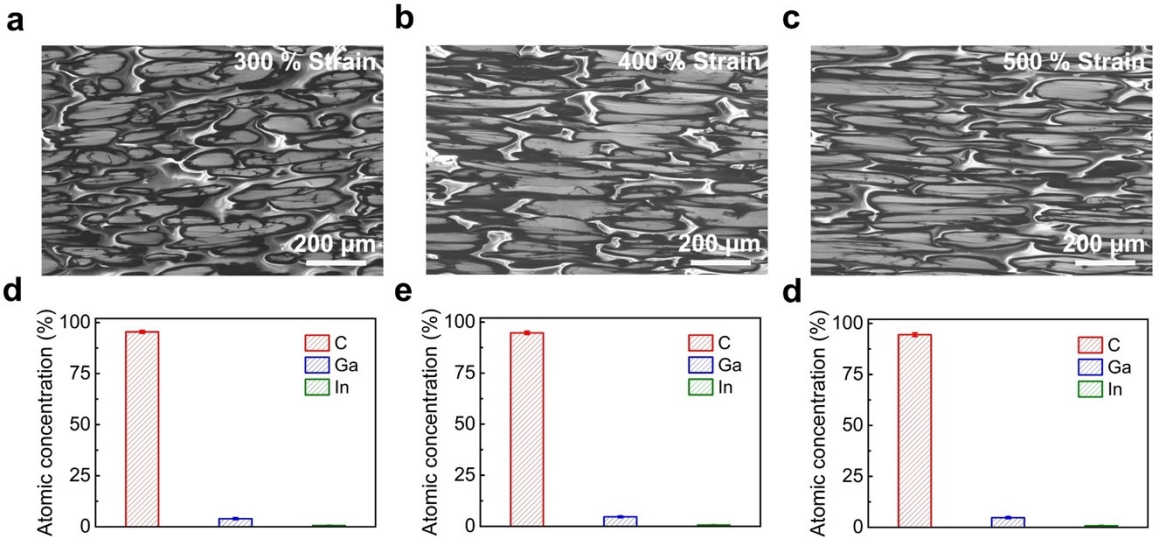

Figure S31. (a)-(c) SEM images of surface morphologies of bilayer interface at sequential tensile strains. (d)-(e) Element atomic concentrations of C, Ga, and In in bilayer interface obtained from EDS results at sequential tensile strains.

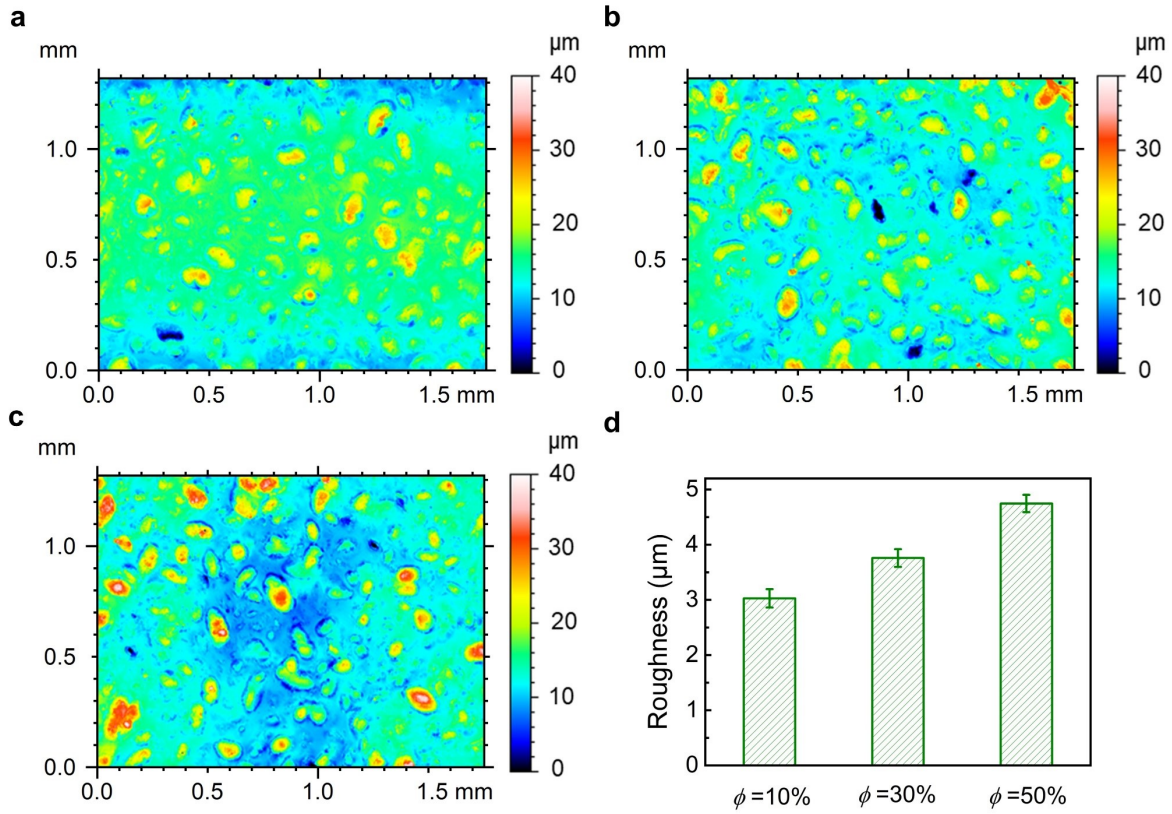

Figure S32. Two-dimensional CLSM images of bilayer interfaces with (a) ϕ = 10%, (b) ϕ = 30%, and (c) ϕ = 50%. (d) Surface roughness of bilayer interfaces with (a) ϕ = 10%, (b) ϕ = 30%, and (c) ϕ = 50%. All the bilayer interfaces have the same particle size of d = 50 μm.

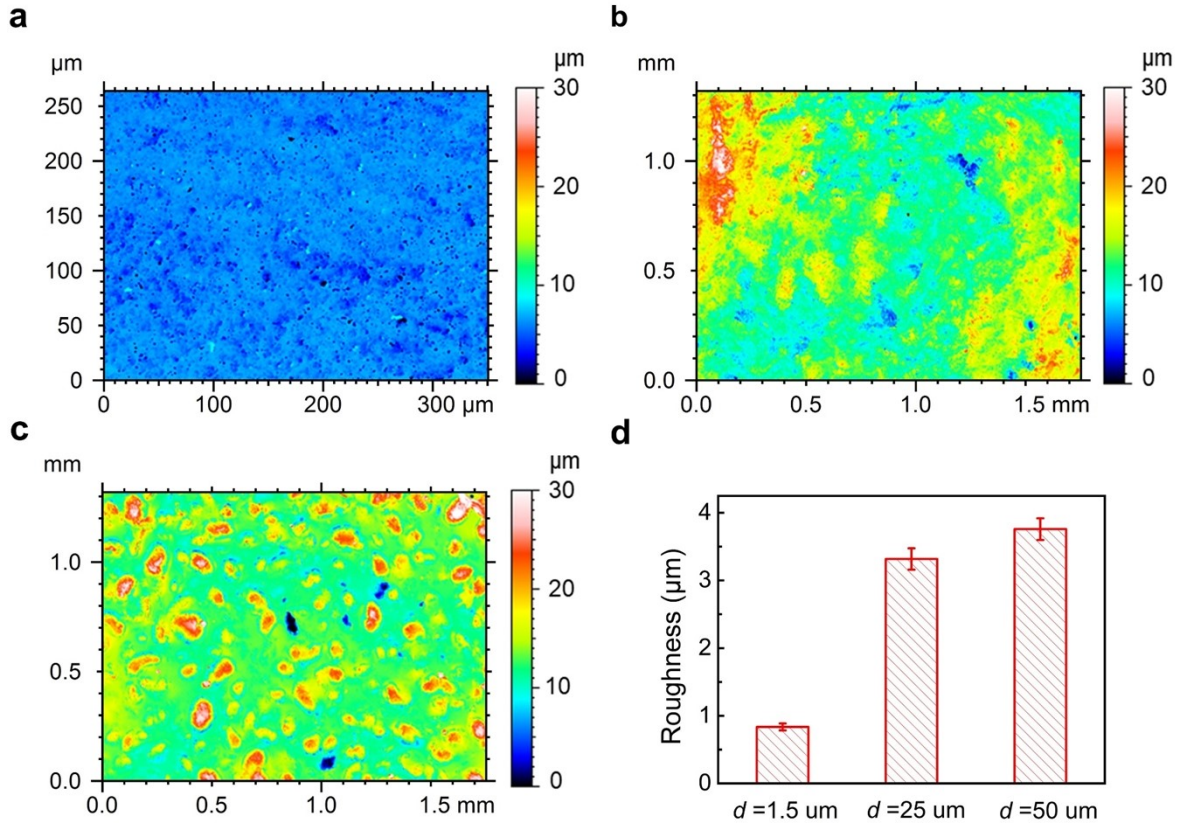

Figure S33. Two-dimensional CLSM images of bilayer interfaces with (a) d = 1.5 μm, (b) d = 25 μm, and (c) d = 50 μm. (d) Surface roughness of the bilayer interfaces with d = 1.5 μm, 25 μm, and 50 μm. All the bilayer interfaces have the same LM volume fraction of ϕ = 30%.

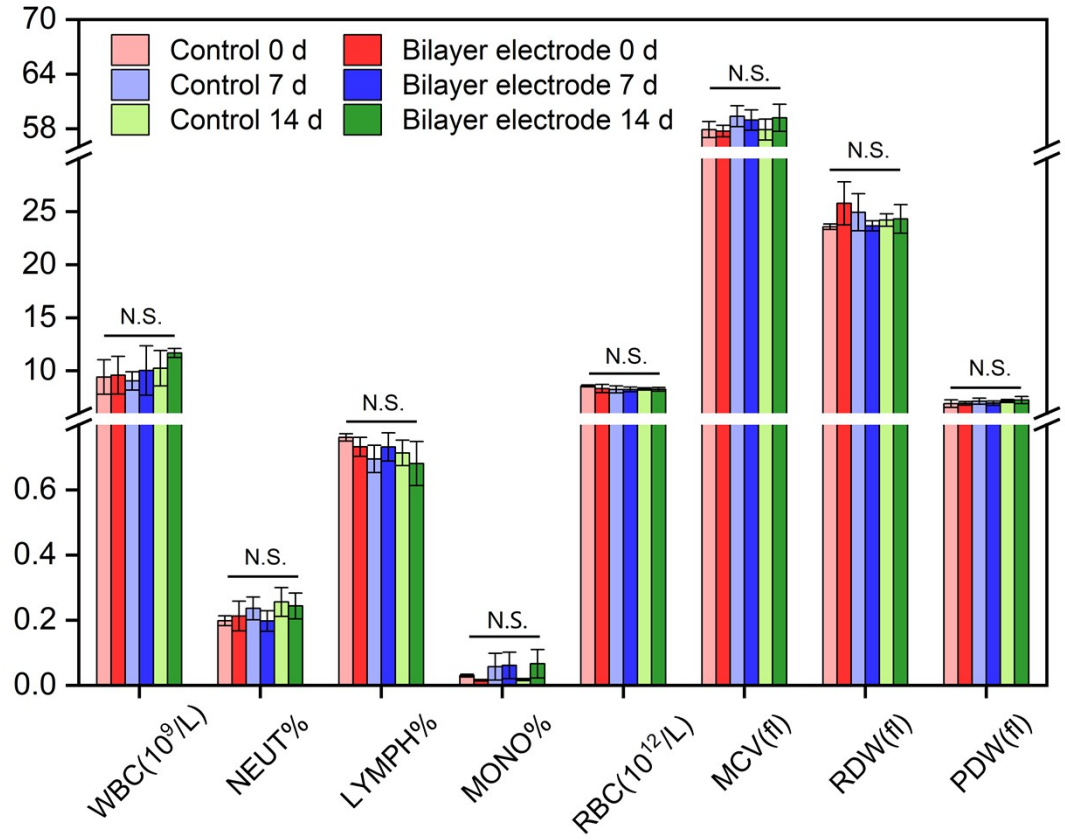

Figure S34. Eight markers (white blood cell count, neutrophil percentage, lymphocyte percentage, monocyte percentage, red blood cell count, mean red blood cell volume, red blood cell distribution width and mean platelet volume) of blood routine of rats in the control group and the bilayer electrode group. The white blood cell count in the treated group shows a slight increase compared to the control group, but this difference is not statistically significant. No significant differences are observed in the percentages of neutrophils, lymphocytes, and monocytes between the treated and control groups over the two-week period, suggesting that the bilayer electrode does not provoke a severe inflammatory response. Furthermore, values of hematological parameters related to red blood cells and platelets exhibit no apparent changes, further supporting the safety and biocompatibility of bilayer electrode.

Figure S35. Digital image of the 2-channel electrode prepared by combining the stencil-printing and the proposed method.

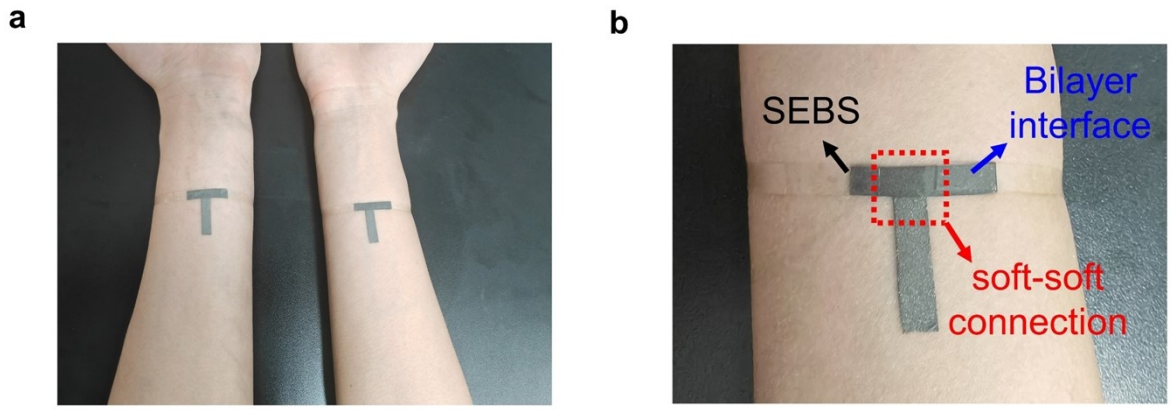

Figure S36. (a) Photographs of the wristbands composed of two bilayer electrodes and a thin SEBS sheet with soft-soft connections. Two wearable wristbands were wrapped around the wrists of the left and right arms of a volunteer. (b) Enlarged view of the wristbands illustrating the self-adhesive and good skin-conformal characteristics.

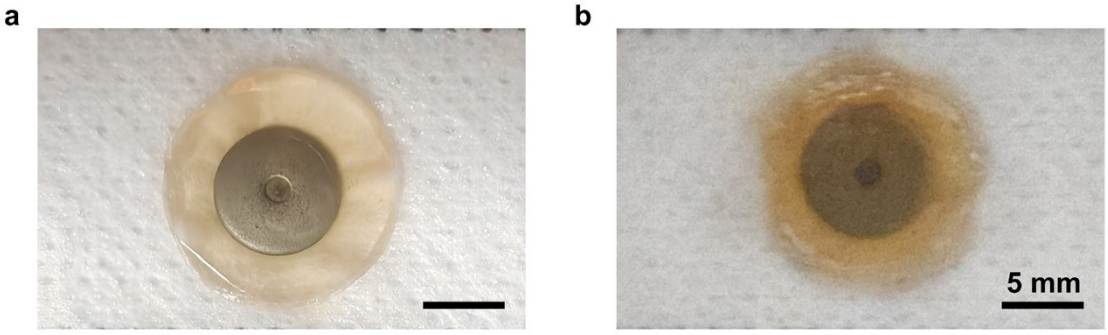

Figure S37. Photographs of commercial Ag/AgCl electrodes after (a) 0 h and (b) 24 hours of wearing.

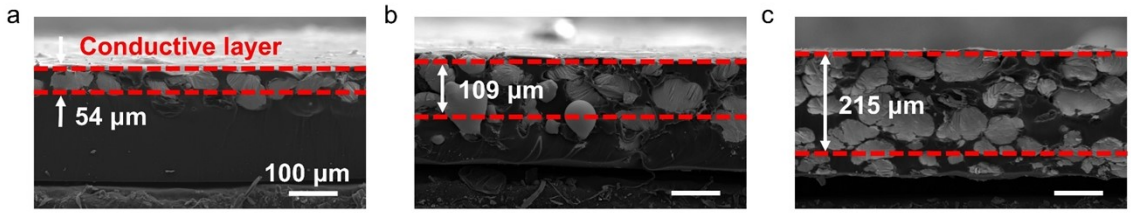

Figure S38. Cross-sectional SEM images of the bilayer interfaces with different LM volume fractions ϕ. (a) ϕ = 10% (b) ϕ = 30% (c) ϕ = 50%.

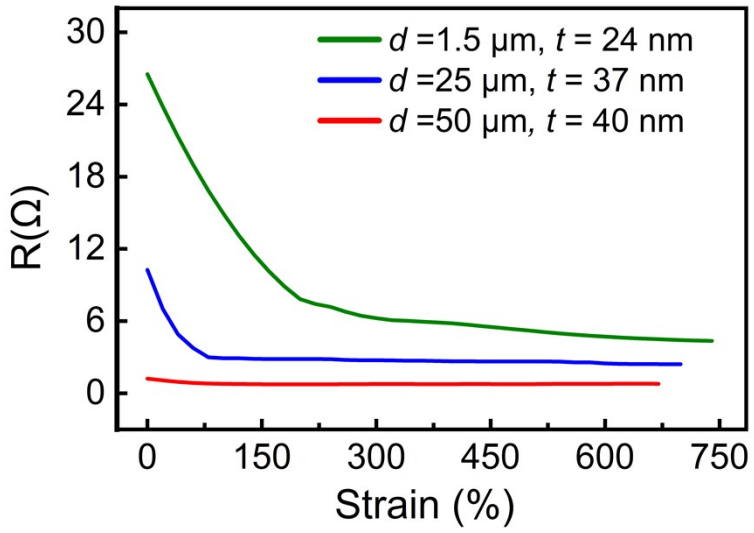

Figure S39. Evolution of resistance with tensile strain for bilayer interfaces with different LM particle diameters *d*. The thicknesses (*t*) of nanoscale SEBS layers were also shown.

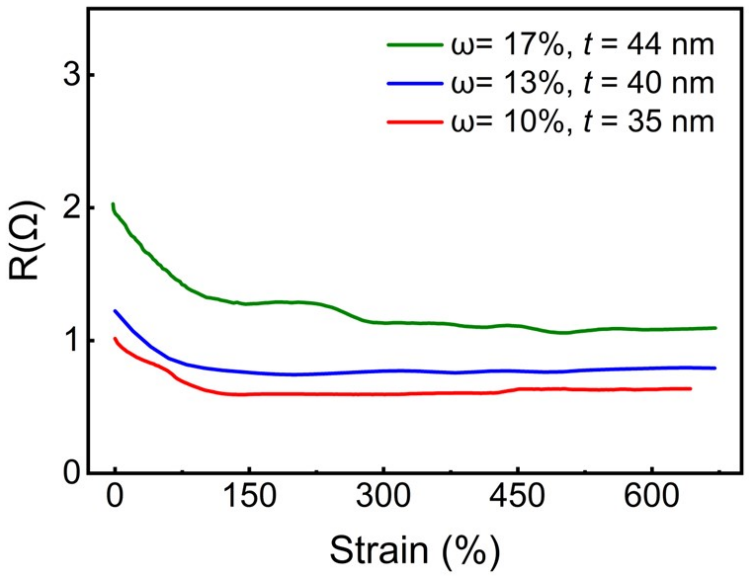

Figure S40. Evolution of resistance with tensile strain for bilayer interfaces with different weight ratios (ω) of toluene to SEBS. The thicknesses (*t*) of nanoscale SEBS layers were also shown.

8. Supplementary information references

1. X. Xue, D. Zhang, Y. Wu, R. Xing, H. Li, T. Yu, B. Bai, Y. Tao, M. D. Dickey and J. Yang, *Adv. Funct. Mater.*, 2022, **33**, 2210553.
2. Y. Liu, X. Ji and J. Liang, *Npj Flex Electron.*, 2021, **5**, 11.
3. F. F. Xie, S. H. Lv, Y. R. Yang and X. D. Wang, *J Phys Chem Lett.*, 2020, **11**, 2818-2823.
4. Z. C. Zhou, Q. Li and X. S. Zhao, *Langmuir.*, 2006, **22**, 3692-3697.
5. Y. I. Rabinovich, M. S. Esayanur and B. M. Moudgil, *Langmuir.*, 2005, **21**, 10992-10997.
6. X. Li, M. Li, J. Xu, J. You, Z. Yang and C. Li, *Nat. Commun.*, 2019, **10**, 3514.
7. L. Shi, Z. Li, M. Chen, T. Zhu and L. Wu, *Adv. Mater.*, 2023, **35**, 2210091.
8. X. W. Zhang, Y. Pan, Q. Zheng and X. S. Yi, *J POLYM SCI POL PHYS*, 2000, **38**, 2739-2749.
9. L. Shi, Z. Li, M. Chen, Y. Qin, Y. Jiang and L. Wu, *Nat. Commun.*, 2020, **11**, 3529.
10. B. B. Tian, J. L. Wang, S. Fusil, Y. Liu, X. L. Zhao, S. Sun, H. Shen, T. Lin, J. L. Sun, C. G. Duan, M. Bibes, A. Barthelemy, B. Dkhil, V. Garcia, X. J. Meng and J. H. Chu, *Nat. Commun.*, 2016, **7**, 11502.
11. Z. Chen, P.-C. Hsu, J. Lopez, Y. Li, J. W. F. To, N. Liu, C. Wang, S. C. Andrews, J. Liu, Y. Cui and Z. Bao, *Nat. Energy*, 2016, **1**, 15009.
12. A. Diaz Lantada, P. Lafont, J. L. Munoz Sanz, J. Manuel Munoz-Guijosa and J. Echavarri Otero, *Sens. Actuators, A*, 2010, **164**, 46-57.
13. R. Tutika, A. B. M. T. Haque and M. D. Bartlett, *Commun. Mater.*, 2021, **2**, 64.
14. H. Wang, Y. Yao, Z. He, W. Rao, L. Hu, S. Chen, J. Lin, J. Gao, P. Zhang, X. Sun, X. Wang, Y. Cui, Q. Wang, S. Dong, G. Chen and J. Liu, *Adv. Mater.*, 2019, **31**, 1901337.
15. B. Deng and G. J. Cheng, *Adv. Mater.*, 2019, **31**, 1807811.
16. C. J. Thrasher, Z. J. Farrell, N. J. Morris, C. L. Willey and C. E. Tabor, *Adv. Mater.*, 2019, **31**, 1903864.
17. S. Liu, D. S. Shah and R. Kramer-Bottiglio, *Nat. Mater.*, 2021, **20**, 851-858.
18. W. Lee, H. Kim, I. Kang, H. Park, J. Jung, H. Lee, H. Park, J. S. Park, J. M. Yuk, S. Ryu, J. W. Jeong and J. Kang, *Science*, 2022, **378**, 637-641.
19. S. Chen, S. Fan, J. Qi, Z. Xiong, Z. Qiao, Z. Wu, J. C. Yeo and C. T. Lim, *Adv. Mater.*, 2023, **35**, 2208569.
20. T. Gan, Q. Xiao, S. Handschuh-Wang, X. Huang, H. Wang, X. Deng, S. Hu, B. Wang, Q. Wu and X. Zhou, *ACS Appl. Mater. Interfaces*, 2022, **14**, 42744-42756.
21. C. Cao, C. Hou, X. Wang, D. Lv, L. Ai, Y. Feng, P. Chen, X. Wang, M. He and X. Yao, *Adv. Funct. Mater.*, 2024, **34**, 2403671.
22. M. Kim, J. J. Park, C. L. Cho and S. H. Ko, *Adv. Funct. Mater.*, 2023, **33**, 2303286.
23. L. Tang, S. Yang, K. Zhang and X. Jiang, *Adv. Sci.*, 2022, **9**, 2202043.
24. L. Tang, L. Mou, J. Shang, J. Dou, W. Zhang and X. Jiang, *Mater. Horiz.*, 2020, **7**, 1186-1194.
25. L. Ding, C. Hang, S. Yang, J. Qi, R. Dong, Y. Zhang, H. Sun and X. Jiang, *Nano Lett.*, 2022, **22**, 4482-4490.
26. S. Chun, D. W. Kim, S. Baik, H. J. Lee, J. H. Lee, S. H. Bhang and C. Pang, *Adv. Funct. Mater.*, 2018, **28**, 1805224.
27. J. Jeon and J.-W. Park, *Nano Lett.*, 2024, **24**, 9553-9560.
28. Y. Ohm, C. Pan, M. J. Ford, X. Huang, J. Liao and C. Majidi, *Nat Electron.*, 2021, **4**, 185-192.
29. Y. Jiang, S. Ji, J. Sun, J. Huang, Y. Li, G. Zou, T. Salim, C. Wang, W. Li, H. Jin, J. Xu, S. Wang, T. Lei, X. Yan, W. Y. X. Peh, S.-C. Yen, Z. Liu, M. Yu, H. Zhao, Z. Lu, G. Li, H. Gao, Z. Liu, Z. Bao and X. Chen, *Nature*, 2023, **614**, 456.
30. P. Tan, H. Wang, F. Xiao, X. Lu, W. Shang, X. Deng, H. Song, Z. Xu, J. Cao, T. Gan, B. Wang and X. Zhou, *Nat. Commun.*, 2022, **13**, 358.
31. L. Zhang, K. S. Kumar, H. He, C. J. Cai, X. He, H. Gao, S. Yue, C. Li, R. C.-S. Seet, H. Ren and J. Ouyang, *Nat.*

1 *Commun.*, 2020, **11**, 4683.
2
3